nature communications

Article

https://doi.org/10.1038/s41467-025-63134-6

Lone pair expression in fluorinated two-dimensional hybrid perovskite enables multiaxial ferroelectricity and nonlinear optical response

Received: 5 March 2025

Accepted: 11 August 2025

Published online: 20 August 2025

Check for updates

Hao-Fei Ni[1,2], Qi-Fang Zhou[1,2], Jia-Qi Luo[1], Gele Teri[1], Lei Pan[1], Lou-Kai Ye[1], Qiang-Qiang Jia[1], Pei-Zhi Huang[1], Pei-Guo Liu[1], Chang-Feng Wang[1], Zhi-Xu Zhang[1] ✉, Da-Wei Fu[1] ✉ & Yi Zhang[1] ✉

Two-dimensional (2D) hybrid organic-inorganic perovskites (HOIPs) with tunable octahedra are promising for flexible devices due to spontaneous-polarization-driven functionalities like ferroelectric memory, piezoelectric sensing and optical switches. However, achieving large spontaneous polarization and strong second harmonic generation (SHG) remains challenging for 2D HOIP ferroelectrics. Here, we report a 2D HOIP ferroelectric (4,4-difluoropiperidinium)$_2$GeBr$_4$ designed by molecular fluorination. Remarkably, (4,4-difluoropiperidinium)$_2$GeBr$_4$ exhibits large saturation polarization (>15 μC/cm^2), high Curie temperature (401 K) and the strongest SHG intensity among 2D HOIP ferroelectrics (about 6.2 times of KH_2PO_4). These properties arise from the synergy of two mechanisms: the 4s^2 lone pair on Ge^{2+} and the orientational ordering of 4,4-difluoropiperidinium cations. Moreover, (4,4-difluoropiperidinium)$_2$GeBr$_4$ features eight equivalent polarization directions (the maximum number among reported 2D HOIP ferroelectrics), enabling its composite (4,4-difluoropiperidinium)$_2$GeBr$_4$@thermoplastic polyurethane device to exhibit prominent piezoelectric sensing. Our work offers a reliable route to high-performance 2D hybrid ferroelectrics and highlights their potential in flexible devices.

Prevailing popularity of hybrid organic-inorganic perovskites (HOIPs) in photovoltaics[1–3] have sparked ever-increasing interest for their great potential in lasing[4], radiation detection[5], ferroelectrics[6], etc[7–9]. Particularly, ferroelectricity, and second harmonic generation (SHG) are crucial properties with strict crystal symmetry dependence, which are essential for a wide array of applications that span from sensing, memory to optical modulation and various life and military uses[10–12]. In recent years, the iterative rise of flexible and wearable applications has put forward new requirements for material attributes[13,14]. Two-dimensional (2D) HOIPs, compared to three-dimensional and one-dimensional counterparts, have attracted tremendous interest as outstanding candidate for flexible devices, by virtue of their natural advantages including highly structural tunability, good material stability, convenient solution processing and excellent ductility of thin films[15–18]. Extensive studies have been dedicated to developing high-performance 2D ferroelectric HOIPs with a series of important

[1]Institute for Science and Applications of Molecular Ferroelectrics, Key Laboratory of the Ministry of Education for Advanced Catalysis Materials, Zhejiang Normal University, Jinhua, People's Republic of China. [2]These authors contributed equally: Hao-Fei Ni, Qi-Fang Zhou. ✉e-mail: zhangzhixu@zjnu.edu.cn; dawei@seu.edu.cn; yizhang1980@zjnu.edu.cn

progress[19–22], such as high Curie temperature[23], high electrocaloric strength[24], unusual birefringence[25] and large piezoelectric response[26]. Nevertheless, the spontaneous polarization (typically <10 μC/cm^2) and SHG intensity, as key performance parameters related to crystal polarity, have long remained at poor levels and been great challenges for 2D ferroelectric HOIPs.

SHG, as one of the most fundamental nonlinear optical processes, requires breaking inversion symmetry, while ferroelectrics must crystallize in a polar point group for generating switchable spontaneous polarization[10,27]. HOIPs closely bridge organic and inorganic components by a well-defined molecular assembly, providing combining merits to endow them with an unrivaled functional design platform[28]. Benefiting from the chemical modifiability of organic molecules, ferroelectrics can be designed rationally through some phenomenological chemical approaches[29–31]. For example, Xiong et al. proposed fluorination strategy that has been demonstrated in some works[32], i.e., enhancing Curie temperature[33], inducing polarity[34], and bring other inspiring physical properties[35]. Besides organic parts, the inorganic components that support the infinitely extended layered skeleton in 2D HOIPs are equally important. Ferroelectric and optoelectronic properties can be optimized by adjusting the inorganic layer thickness and interlayer distance of 2D HOIPs[36,37]. Constructing specific metal halide octahedra can also endow additional fascinating properties[38–40]. Emphatically, what truly interests us is the germanium-based perovskites, whose strong stereochemical activity of the 4s^2 lone pair electrons that will result in strong octahedral distortion and off-centering, and contribute supplemental electron polarization[41–43]. Boosted by the stereochemical lone pair electrons expression of Ge^{2+} ions, for instance, robust ferroelectric polarization has been excavated in three-dimensional $CsGeX_3$ (where X = Cl, Br and I)[44] and our reported one-dimensional (dimethylammonium)GeI_3[45]. Recently, Liu et al. reported 2D Ge-based HOIP ferroelectric and antiferroelectric with large polarization and great photoelectric properties though the rational utilization of 4s^2 lone pair electrons[46,47]. Strong SHG responses have also been revealed in several Ge-based HOIPs[48–50]. However, ferroelectricity has been largely unexplored in 2D Ge-based HOIPs yet, and the ones simultaneously with large saturation polarization and strong SHG response remain blank. Taking the structural features of superior chemical modifiability and pronounced lone pair stereochemical expression of 2D Ge-based HOIPs, it's time to open this Pandora's box to develop high-performance ferroelectric properties.

Herein, inspired by the aforementioned ideas, we present a two-dimensional germanium halide perovskite ferroelectric (4,4-DFPD)$_2GeBr_4$ (4,4-DFPD is 4,4-difluoropiperidinium) designed by a molecular fluorination strategy. Compared to (piperidinium)$GeBr_3$, the fluorination effect enables organic cations to be stabilized in a 2D confined space with an orientational ordering manner, resulting in polar crystal symmetry for (4,4-DFPD)$_2GeBr_4$. Remarkably, its lone pair stereochemical activity in Ge^{2+} ions induces large off-centering displacement and supplemental electron polarization, together with fluorination-enhanced molecular dipole moments, facilitate a large saturation polarization of 15.85 μC/cm^2, which is much higher than most of reported 2D hybrid perovskite ferroelectrics. More strikingly, these structural attributes of (4,4-DFPD)$_2GeBr_4$ further brings about extremely strong SHG response with polarization-dependent notable anisotropy, whose intensity is the highest one in 2D hybrid perovskite family so far (about 6.2 times that of classical KH_2PO_4). (4,4-DFPD)$_2GeBr_4$ also possesses multiaxial characteristics with eight equivalent polarization directions, which is the maximum number among the reported 2D hybrid perovskite ferroelectrics. Combined with the multiaxial characteristics, facile solution processing and easy film-forming, we further demonstrated the prominent piezoelectric sensing and optical modulation functions of (4,4-DFPD)$_2GeBr_4$ in its polycrystalline composite form, showing great application prospects in flexible multifunctional devices.

Results

Structural analysis of crystals

H/F substitution serves as an effective chemical strategy to enhance molecular dipole moments and induce orientational ordered alignment within lattice (Fig. 1 and Supplementary Fig. 1). Herein, we performed H/F substitution on the piperidine (PD) molecule to obtain monofluoro-substituted 4-fluoropiperidine (4-FPD) and difluoro-substituted 4,4-difluoropiperidinium (4,4-DFPD) cations. The single crystal samples were synthesized in HBr solution containing stoichiometric amounts of GeO_2 and the corresponding organic amine via programmed temperature control (see more details in crystal synthesis and growth). Single-crystal X-ray diffraction (SC-XRD) reveals that (PD)$GeBr_3$ adopts a typical one-dimensional (1D) HOIP structure with centrosymmetric $P2_1/n$ space group (Supplementary Fig. 2a and Supplementary Table 1). Structurally, the strong lone pair stereochemical expression of the Ge^{2+} ion induces two distinct Ge-Br bond lengths, which result in a significant distortion of $[GeBr_6]^{4-}$ octahedron (Supplementary Fig. 2b). In terms of molecular packing pattern, (4-FPD)$GeBr_3$ maintains identical structural characteristics to (PD)$GeBr_3$ (Supplementary Fig. 3 and Supplementary Table 1). Compared with (PD)$GeBr_3$, (4-FPD)$GeBr_3$ exhibits more significant octahedral elongation (Δd) and angle variances (σ^2_{oct}), indicating enhanced stereochemical activity (Supplementary Fig. 4a). These structural variations originate from the larger dipole moment and steric hindrance of

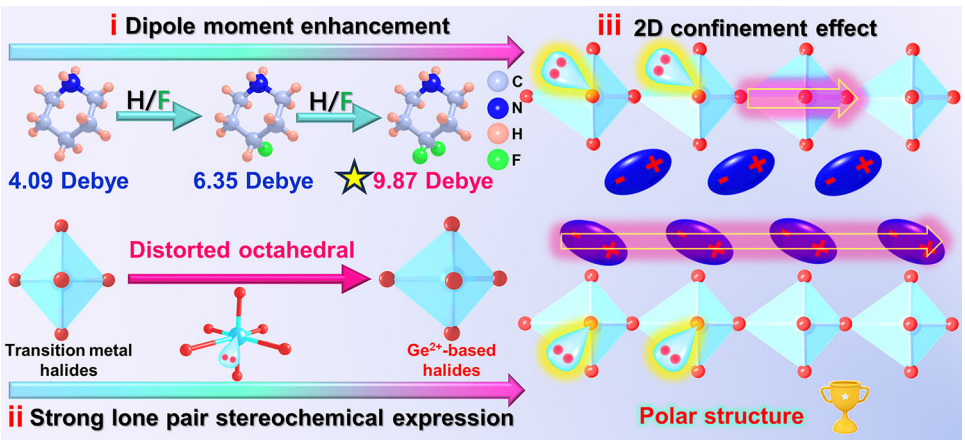

Fig. 1 | Designing strategy. Diagram of designing 2D Ge-based halide perovskite ferroelectric (4,4-DFPD)$_2GeBr_4$. Since the lone pair electrons repels the bonding electrons, as a result it is located on the three longer Ge-Br bonds, thus giving the octahedron a strong structural distortion.

https://doi.org/10.1038/s41467-025-63134-6

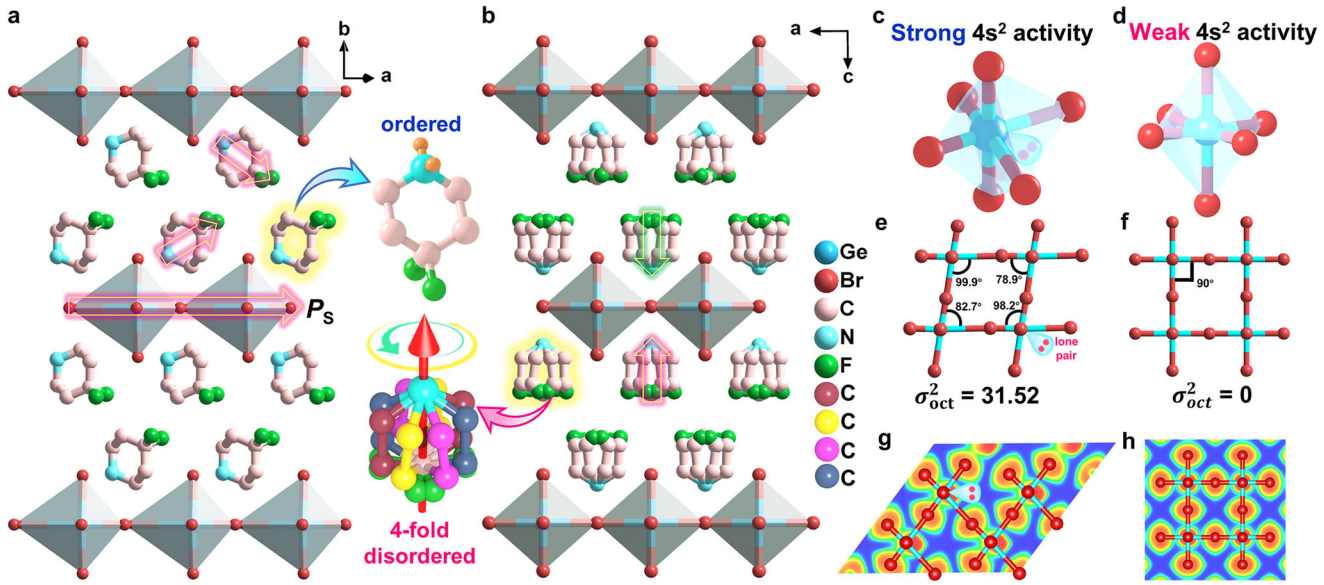

Fig. 2 | Crystal structures of (4,4-DFPD)$_2$GeBr$_4$. Packing view of (4,4-DFPD)$_2$GeBr$_4$ at **a** 273 K and **b** 407 K. The 4s^2 lone pair electrons activity of [GeBr$_6$]$^{4-}$ octahedron at **c** 273 K and **d** 407 K. Geometrical parameter of 2D [GeBr$_4$]$^{2-}$ layer at **e** 273 K and **f** 407 K. Electron localization function (ELF) maps at **g** LTP and **h** HTP project on the plane of 2D layer. The hydrogen on the C and N atoms were omited for clarity. The lone pair electrons repel the bonding electrons, resulting in two distinct Ge–Br bond lengths and structural polarization in octahedron.

fluorinated organic cations. From the packing view, the 4s^2 lone pairs on Ge^{2+} ions induce distorted octahedra with antiparallel arrangements along 1D chains (Supplementary Fig. 4b). Combined with analogous organic cation packing modes, this produces zero macroscopic spontaneous polarization within lattice. Additionally, thermogravimetric analysis indicates both (PD)GeBr$_3$ and (4-FPD)GeBr$_3$ exhibit good thermal stability (Supplementary Fig. 5).

In view of this, we further synthesized (4,4-DFPD)$_2$GeBr$_4$ that crystallized in the polar *m* point group at 273 K (Supplementary Table 2). The 4,4-DFPD cations act as interlayer spacers that stabilize the 2D HOIP structure. (4,4-DFPD)$_2$GeBr$_4$ adopts a Ruddlesden–Popper type 2D HOIP structure, where the 2D confinement effect modulates lone pair stereochemical expression within distorted [GeBr$_6$]$^{4-}$ octahedra, enabling orientational ordered arrangement within the inorganic layers (Fig. 2a, c). Concurrently, interlayer 4,4-DFPD cations adopt polar packing featured with uniform C-F bond orientation within (0 1 0) plane. The synergistic alignment of these two structural components generates non-zero spontaneous polarization in-plane that is parallel to the inorganic layer (Supplementary Fig. 6). Powder X-ray diffraction (PXRD) patterns of (4,4-DFPD)$_2$GeBr$_4$ match perfectly with the simulated results, confirming phase purity and testing accuracy of polycrystalline powder samples in the subsequent characterization (Supplementary Fig. 7). Additionally, the PXRD patterns remain unchanged after exposure to air for 30 days, proving its environmental stability (Supplementary Fig. 8).

To investigate the phase transition behaviors of (4,4-DFPD)$_2$GeBr$_4$, we carried out differential scanning calorimetry (DSC) testing. The DSC curves reveal two pairs of reversible thermal anomalies during heating-cooling cycles, confirming reversible phase transitions at 361 and 400 K (Supplementary Fig. 9a). For clarity, we label the phases below 361 K and above 400 K as the low-temperature-phase (LTP) and high-temperature-phase (HTP), respectively, while the phase between these two is the intermediate-temperature phase (ITP). Notably, thermogravimetric analysis of (4,4-DFPD)$_2$GeBr$_4$ shows a decomposition temperature (418 K) exceeding the phase transition temperature (Supplementary Fig. 9b). However, this temperature is close to the ITP-to-HTP phase transition point, which results in poor diffraction data quality of HTP due to thermal fluctuations and highly molecular disorder, synergistically amplifying background scattering signal. At 370 K in ITP, (4,4-DFPD)$_2$GeBr$_4$ remains crystallized in the polar *m* point group. The refined structure shows that slight orientational disorder of F atoms is responsible for this phase transition (Supplementary Fig. 10). At 407 K in HTP, (4,4-DFPD)$_2$GeBr$_4$ crystallized in the centrosymmetric *I*4/*mmm* space group (Fig. 2b and Supplementary Table 2), featuring regular [GeBr$_6$]$^{4-}$ octahedra with weakened stereochemical activity (Fig. 2d). In contrast, strong lone pair expression in LTP distorts the [GeBr$_6$]$^{4-}$ octahedron to reach a lower energy state, increasing the value of Δd by an order of magnitude compared to HTP (Supplementary Fig. 11). As shown in Supplementary Fig. 12 and Supplementary Table 3, the full width at half maximum of the Raman peak near 173 cm^{-1} increases substantially, suggesting that the Ge-Br bond experiences a pronounced symmetrical stretching vibration during the transition of (4,4-DFPD)$_2$GeBr$_4$ to the high-temperature phase. In LTP, strong stereochemical expression in distorted octahedron (σ^2_{oct} = 31.52) repels the bonding electron pairs, generating macroscopic polarization within layers (Fig. 2e, g). While for HTP, the regular octahedra (σ^2_{oct} = 0) cancel this macroscopic polarization due to a relatively weak lone pair stereochemical expression of Ge^{2+} ions (Fig. 2f, h). Concomitantly, 4,4-DFPD cations in HTP are located on special site 4 *mm*. Unlike the well-ordered 4,4-DFPD cations in LTP, these cations adopt a 4-fold orientational disorder state in HTP, canceling molecular dipole with each other at a position perpendicular to the 4-fold axis (Fig. 2b). Due to the highly disorder of the 4,4-DFPD cations, deviations of the C–F bond angles from the ideal molecular geometry are observed in the refined structure. Accurately modeling and distinguishing the atomic positions becomes challenging in the refinement of the highly disordered high-temperature phase, where extensive dynamic disorder and partial occupancies obscure individual atomic sites[51–56]. Such an order-disorder transition belongs to a 4/*mmm*F*m* ferroelectric phase transition, accompanied by symmetry elements decrease from 16 (E, $2C_4$, C_2, i, $2S_4$, σ_h, $2\sigma_v$, $2\sigma_d$, $2C_2'$, $2C_2''$) to 2 (E, σ_h) (Supplementary Fig. 13). Remarkably, this symmetry breaking process endows (4,4-DFPD)$_2$GeBr$_4$ with eight equivalent polarization directions, representing the maximum number among reported 2D HOIP ferroelectrics (Supplementary Fig. 14 and Supplementary Table 4). We attribute the origin of its multiaxial

https://doi.org/10.1038/s41467-025-63134-6

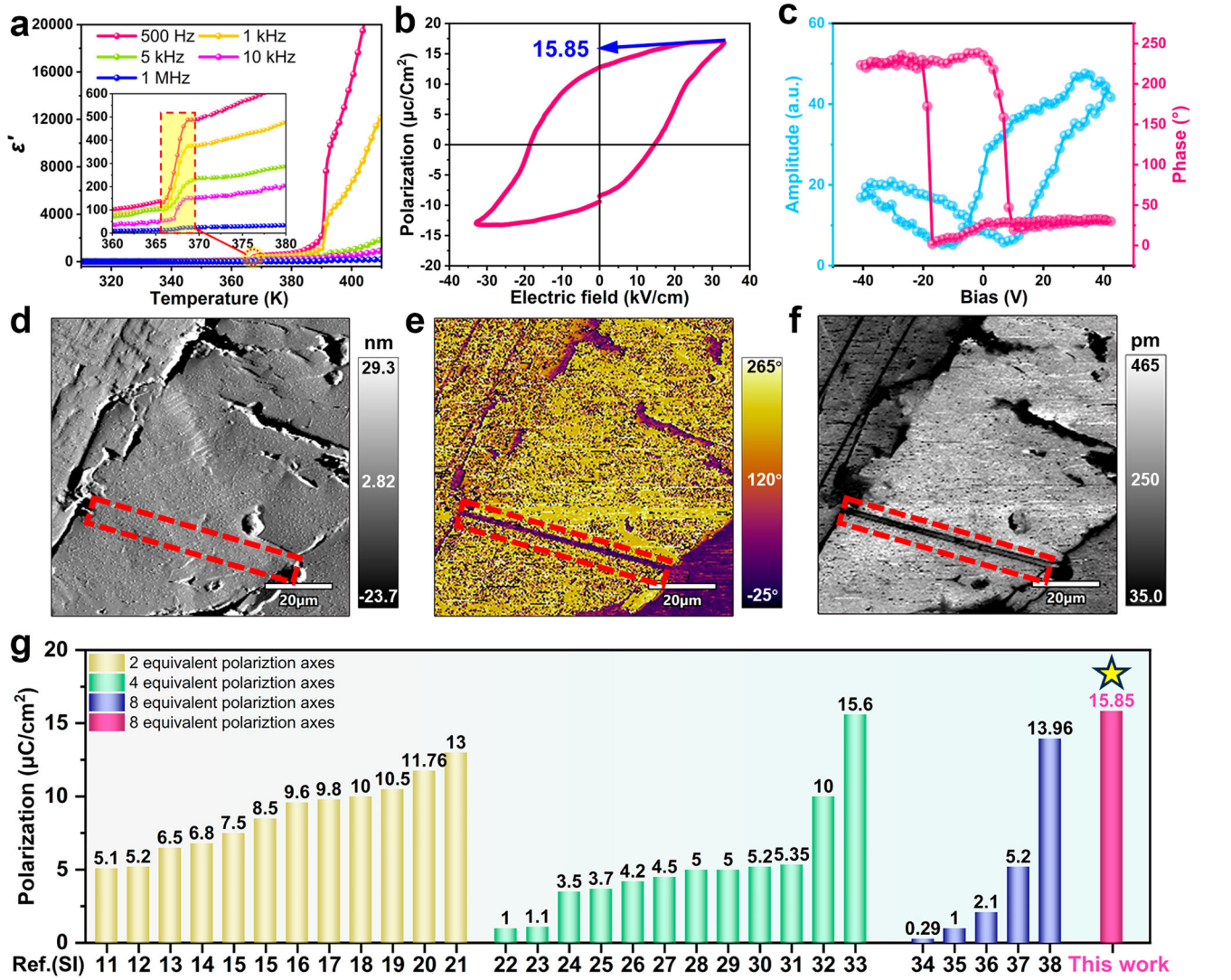

Fig. 3 | DSC, SHG, dielectric properties and ferroelectricity of $(4,4\text{-DFPD})_2GeBr_4$. **a** Temperature-dependent real part of the complex dielectric constant at frequency of 500 Hz to 1 MHz. **b** *P–E* hysteresis loops measured at room temperature. **c** Hysteretic loops of Piezoresponse force microscopy (PFM) phase and amplitude with bias voltage. **d–f** PFM morphology, phase and amplitude images of $(4,4\text{-DFPD})_2GeBr_4$ polycrystalline thin film. **g** Comparison of polarization axes and values between $(4,4\text{-DFPD})_2GeBr_4$ and other 2D HOIPs ferroelectrics. The ref. (SI) in **g** corresponds to the references in Supplementary Information.

ferroelectricity to the lower symmetry in the ferroelectric phase due to the strong stereochemical lone pair expression of Ge^{2+} ions in the octahedral unit. Additionally, the Curie temperature of $(4,4\text{-DFPD})_2GeBr_4$ (401 K) is higher than that of most reported ferroelectrics, as well as Ge-based 2D ferroelectrics like $AA_2CsGe_2I_7$, ensuring their stable ferroelectricity under environmental conditions (Supplementary Table 5)[47].

Characterization of ferroelectricity

Typically, ferroelectrics could show significant anomalies in dielectric behavior near the Curie temperature. We confirmed the orientation of the crystals by morphology simulation and carried out the dielectric testing along the crystallographic *c*-axis (Supplementary Fig. 15). As revealed by the dielectric response, a steep step-shaped dielectric anomaly occurred at 393.9 K accompanied by a significant value change in ε' from 885 to 11216 at 500 Hz (Fig. 3a). In contrast, the temperature-dependent dielectric constant shows a relatively flat anomaly (from 128 to 489) at 365.9 K, indicating a slight structural change (Fig. 3a). For a ferroelectric, the polarization (*P*)-electric field (*E*) hysteresis loop is the most direct evidence. By testing the single crystal at room temperature, a well-defined nonlinear *P-E* hysteresis loop was obtained, demonstrating the switching process of spontaneous polarization (Fig. 3b). Notably, $(4,4\text{-DFPD})_2GeBr_4$ possesses a large saturation polarization (P_s) up to 15.85 μC/cm², which is ascribed to the obvious structure distortion caused by $4s^2$ lone pair electrons activity of Ge^{2+} ions. This P_s value is larger than that most of the reported 2D hybrid perovskite ferroelectrics (Fig. 3g and Supplementary Table 4). It also possesses multiaxial characteristics with eight equivalent polarization orientations, which is the maximum one among the reported 2D hybrid perovskite ferroelectric, whose majority are uniaxial or biaxial. Additionally, the number of polarization orientations for the typical inorganic perovskite ferroelectric $BaTiO_3$ is equal to or less than three. Combined with the excellent ductility of 2D HOIPs in thin film, it is expected to enable applications in flexible electronics. Then, we carried out a piezoresponse force microscopy (PFM) measurement on polycrystalline thin films to analyze micro domain structure. PXRD results of the thin film show that several strong diffraction peaks at specific crystal faces match well with those obtained by fitting the crystal data, indicating an out-of-plane preferred orientation (Supplementary Fig. 16). A typical butterfly loop of amplitude and obvious hysteresis behavior in the phase signal provides evidence for switching polarization (Fig. 3c). Moreover, the

https://doi.org/10.1038/s41467-025-63134-6

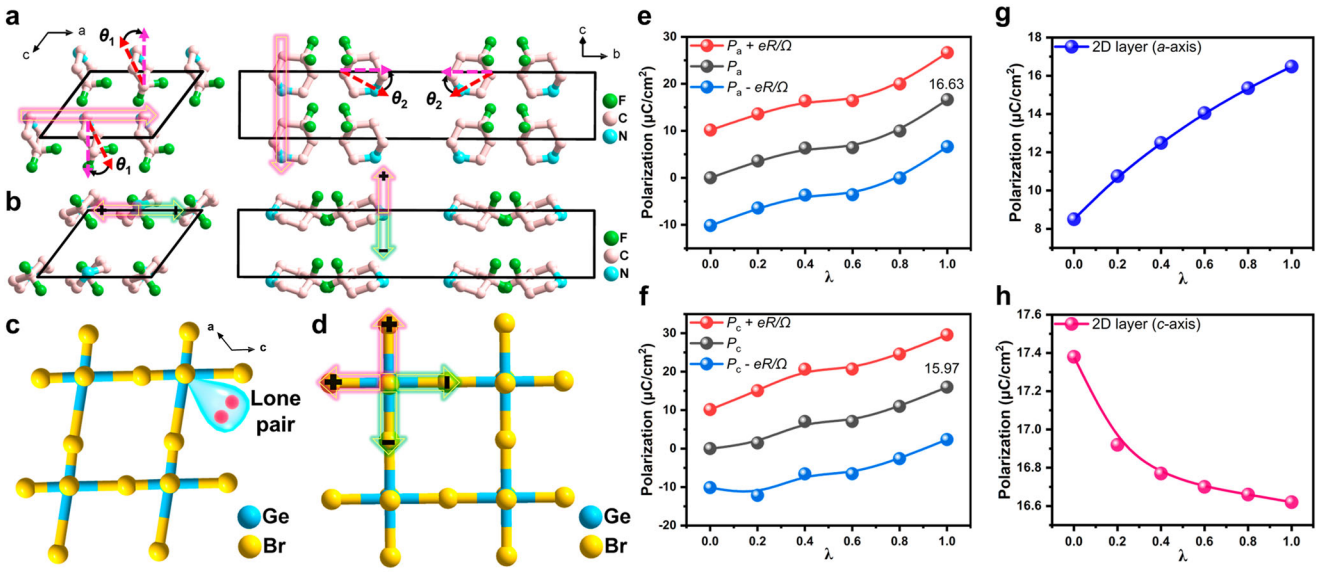

Fig. 4 | Density functional theory (DFT) calculations of $(4,4\text{-DFPD})_2GeBr_4$. **a**, **b** Packing view of 4,4-DFPD cations at ferroelectric configuration ($\lambda = 1$) and paraelectric configuration ($\lambda = 0$). θ_1 and θ_2 represent the rotation angle of 4,4-DFPD cations in plane that parallel and perpendicular to the 2D layer for modeling dynamic path. **c**, **d** 2D $[GeBr_4]^{2-}$ skeleton at $\lambda = 1$ and $\lambda = 0$. **e**, **f** Evolution of polarization along crystallographic *a* and *c*-axis as a function of the dynamic path connecting the $\lambda = 1$ to $\lambda = 0$. **g**, **h** The 2D inorganic layer transform from the ferroelectric state to the paraelectric state with organic cations are kept in the ferroelectric state. Lone pairs electrons located in the 2D layer enhance the polarization along the crystallographic *a*-axis.

long strip-shaped domain structure and clear domain boundaries were observed with no crosstalk between the domain pattern and the sample morphology, revealing robust ferroelectricity of polycrystalline thin films (Fig. 3d–f).

To gain a deeper insight into the atomistic structure evolution of ferroelectric phase transition and large spontaneous polarization, we carried out the density functional theory (DFT) calculations (Supplementary Note 1). The construction of the polarization dynamic path from ferroelectric ($\lambda = 1$) to paraelectric ($\lambda = 0$) configuration is crucial, which strictly follows the evolution of crystal symmetry. For the ferroelectric phase, the crystal symmetry of the *m* point group results in two components along the crystallographic *a*- and *c*-axes, respectively. Therefore, the building of dynamic path should simultaneously consider different orientation state of 4,4-DFPD cations within plane that are parallel and perpendicular to the 2D layer to ensure the zero-polarization state at $\lambda = 0$ (Fig. 4a, b). Meanwhile, Ge^{2+} and Br^- ions in $[GeBr_6]^{4-}$ octahedron experience a displacement to cancel the spontaneous polarization within 2D layer (Fig. 4c, d). Compared to the slight displacement observed in most reported 2D HOIPs ferroelectrics, the geometric parameter of $[GeBr_6]^{4-}$ octahedron undergo a relatively significant changes. This is due to the obvious structural distortion caused by strong lone pair stereochemical expression of Ge^{2+} ions in ferroelectric phase. Thus, we can anticipate that the $[GeBr_6]^{4-}$ octahedron will produce a considerable contribution to the large polarization. As shown in Fig. 4e, f, the polarization value undergoes smooth changes during the switching process from $\lambda = 1$ to 0, in which the theoretical polarization values of $(4,4\text{-DFPD})_2GeBr_4$ are calculated as 15.97 and 16.63 μC/cm² along the crystallographic *a* and *c*-axis, respectively. Additionally, the branches are separated by the polarization quantum when a quantum polarization is added or subtracted (Fig. 4e, f). Specifically, at $\lambda = 1$, the polarization quantum values are 13.61 μC/cm² along the crystallographic *c*-axis and 10.01 μC/cm² along the crystallographic *a*-axis, whereas at $\lambda = 0$, the value is 10.15 μC/cm² along both the crystallographic *a*- and *c*-axes. To quantify the contribution of the 2D inorganic layer to the total polarization, we kept the 4,4-DFPD cations in the ferroelectric state while gradually restoring the 2D inorganic layer from the ferroelectric to the paraelectric state. Although this calculation method does not account for the feedback effects of induced polarization from organic cations, the proposed mechanism remains theoretically sound and is supported by experimental observations[57]. As shown in Fig. 4g, h, and 2D layer exhibits a polarization values of −0.76 and 7.98 μC/cm² along crystallographic *c*- and *a*-axes, respectively. Especially along the crystallographic *a*-axis, the inorganic octahedral skeleton contributes up to half of the overall polarization value. This is due to the strong $4s^2$ lone pair expression of Ge^{2+} ions enhance the structrual polarization along crystallographic *a*-axis (Fig. 4c). We further analyzed the electron localization function (ELF) maps projected on the plane parallel to the 2D octahedra layers. From $\lambda = 1$ to 0, the $4s^2$ lone pair electrons gradually changed from a strong stereochemical expression into a weak one, which is consistent with a smooth change in polarization value to zero at $\lambda = 0$ (Supplementary Fig. 17).

Nonlinear optical response

Ultraviolet–visible-NearInfrared (UV–Vis-NIR) spectra confirmed a strong absorption edge at 422 nm for $(4,4\text{-DFPD})_2GeBr_4$, and the Tauc plot reveals an optical band gap of 3.07 eV (Supplementary Fig. 18). Furthermore, we performed DFT calculations to investigate the energy band structure of $(4,4\text{-DFPD})_2GeBr_4$. The results show that $(4,4\text{-DFPD})_2GeBr_4$ has a direct bandgap of 2.76 eV, where the valence band maximum (VBM) and conduction band minimum (CBM) are located at the same point in the Brillouin zone (Supplementary Fig. 19a). The calculated band gap is slightly lower than the experimental one, due to the limitation of the Perdew–Burke–Ernzerhof exchange–correlation functional. Partial density of states analysis reveals that the 2D inorganic layers govern the electronic band structure of the material. The CBM primarily originates from hybridized Ge-4s/4p and Br-4p orbitals, and the VBM is dominated by Ge-4p orbitals (Supplementary Fig. 19b).

Polar crystals with breaking inversion centers naturally exhibit SHG responses, which, as a second-order nonlinear optical process, allow two photons with the same frequency to effectively convert into a new photon with twice the frequency. Additionally, we collected crystal data with a longer detector exposure time. The Wilson plot and the cumulative intensity of $(4,4\text{-DFPD})_2GeBr_4$ suggest that the structure tends to be non-centrosymmetric (Supplementary Fig. 20 and

https://doi.org/10.1038/s41467-025-63134-6

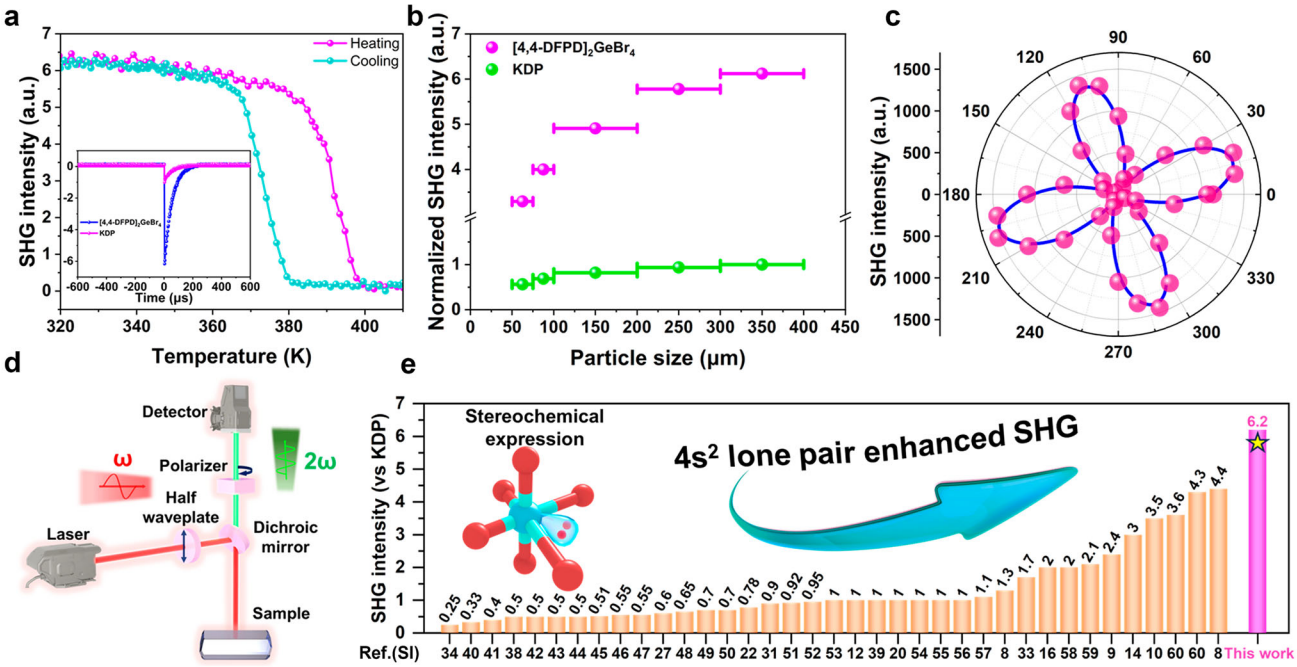

Fig. 5 | The SHG response of $(4,4\text{-DFPD})_2GeBr_4$ under 1064 nm laser radiation. **a** The temperature-dependent SHG intensity of $(4,4\text{-DFPD})_2GeBr_4$ polycrystalline samples. Inset: the comparison of SHG signals between $(4,4\text{-DFPD})_2GeBr_4$ and KDP. **b** The SHG intensity of $(4,4\text{-DFPD})_2GeBr_4$ and KDP as a function of particle size. Error bars represent the measurement uncertainty of particle size: ±12.5 μm for 62.5 and 87.5 μm, and ±50 μm for 150, 250 and 350 μm. **c** The SHG anisotropic polar plot of $(4,4\text{-DFPD})_2GeBr_4$ crystal. **d** The schematic diagram of SHG anisotropic testing. **e** Comparison of SHG intensity between $(4,4\text{-DFPD})_2GeBr_4$ and other 2D HOIPs. The Ref.(SI) in **e** corresponds to the references in Supplementary Information.

Supplementary Table 6). To further confirm the polar structure of $(4,4\text{-DFPD})_2GeBr_4$, we conducted SHG experiments on the polycrystalline powder samples, and the results show a strong SHG signal at room temperature, confirming its non-centrosymmetric nature in LTP (Fig. 5a). The SHG intensity versus the pumped power is fitted with a slope of around 2.02, indicating a two-photon mechanism in $(4,4\text{-DFPD})_2GeBr_4$ (Supplementary Fig. 21). Furthermore, the SHG intensity begins to decrease when the pumped power is greater than 85 mW, which can be considered the laser damage threshold (Supplementary Table 7). With increasing temperature, SHG signal remains in an active state within LTP while its intensity drops down to zero above T_C, entering the paraelectric phase (HTP) with a centrosymmetric structure (Fig. 5a). The SHG intensity of $(4,4\text{-DFPD})_2GeBr_4$ is positively correlated with the particle size of crystal samples (phase matchable) (Fig. 5b). At a particle size scale of about 250 μm, the SHG intensity of $(4,4\text{-DFPD})_2GeBr_4$ is greater than those reported in other 2D HOIPs (Supplementary Table 8). Interestingly, the SHG testing on bulk single crystal further reveals notable anisotropy of response related to the direction vector of polarization. Figure 5d depicts the schematic diagram of the experimental equipment, and the relationship between the SHG intensity and the polarization angle was obtained from a series of spectra under different angle values in a polarization sweep, showing a clear angle-dependent quadruple-polar behavior. Specifically, the SHG intensity varies with the polarization angle and reaches its highest and lowest points with an interval of about 90° (Fig. 5c). It is worth mentioning that the SHG strength of $(4,4\text{-DFPD})_2GeBr_4$ (polycrystalline powder sample) is 6.2 times that of KDP, greatly higher than that of all the reported 2D hybrid perovskite ferroelectrics so far (Fig. 5e).

Piezoelectric sensing performance

Besides large polarization and strong SHG response, $(4,4\text{-DFPD})_2GeBr_4$ also possesses multiaxial characteristics with eight equivalent polarization orientations, which endows its polycrystalline products with excellent piezoelectric sensing performance while not requiring bulk crystals. To measure the intrinsic piezoelectric coefficient of $(4,4\text{-DFPD})_2GeBr_4$, we carried out a quasi-static method on its bulk single crystal and obtained a longitudinal piezoelectric coefficient d_{33} value of 20.9 pC/N along crystallographic the *c*-axis direction (Fig. 6a and Supplementary Fig. 22). The d_{33} value of $[4,4\text{-DFPD}]_2GeBr_4$ is at a medium-high level and its multiaxial characteristics also enable the composite film to exhibit excellent piezoelectric sensing (Supplementary Table 5). Considering these properties, we fabricate a piezoelectric sensor device with a sandwich structure based on a composite polycrystalline thin film containing $(4,4\text{-DFPD})_2GeBr_4$ and thermoplastic polyurethane (TPU) (Fig. 6b). PXRD data confirmed that $(4,4\text{-DFPD})_2GeBr_4$ was successfully dispersed into TPU with a random orientation (Supplementary Fig. 23). Different from uniaxial ferroelectrics in which the application is confined to the specific orientation of the single crystal, its multiaxial characteristic provides an advantage for piezoelectric sensing applications in composite thin films. Moreover, it retained phase stability after exposure to air for 30 days (Supplementary Fig. 24). As shown in Fig. 6c, when subjected to repeated external forces of approximately 10 N, the composite device shows a stable peak-to-peak output voltage of around 9 V. Given the stable output and good sensitivity, the composite film was fixed on the knuckle of the glove to capture the signal output generated by finger bending and then perform analysis for gesture recognition (Fig. 6b and Supplementary Fig. 25). During the process of making gestures, five consecutive segments of signals from different fingers were collected to accurately identify specific finger bending (Fig. 6d, e). For example, when we make an "OK" gesture with thumb and index finger flexion, we can detect a voltage output signal from the corresponding fingers in response (Gesture 2 in Fig. 6d, e). The similar behaviors were also realized by inputting different gestures 1, 3 and 4, proving the good sensitivity and applicability for gesture recognition (Fig. 6d, e). These attributes make the $(4,4\text{-DFPD})_2GeBr_4$ have great potential to enable human–machine interaction.

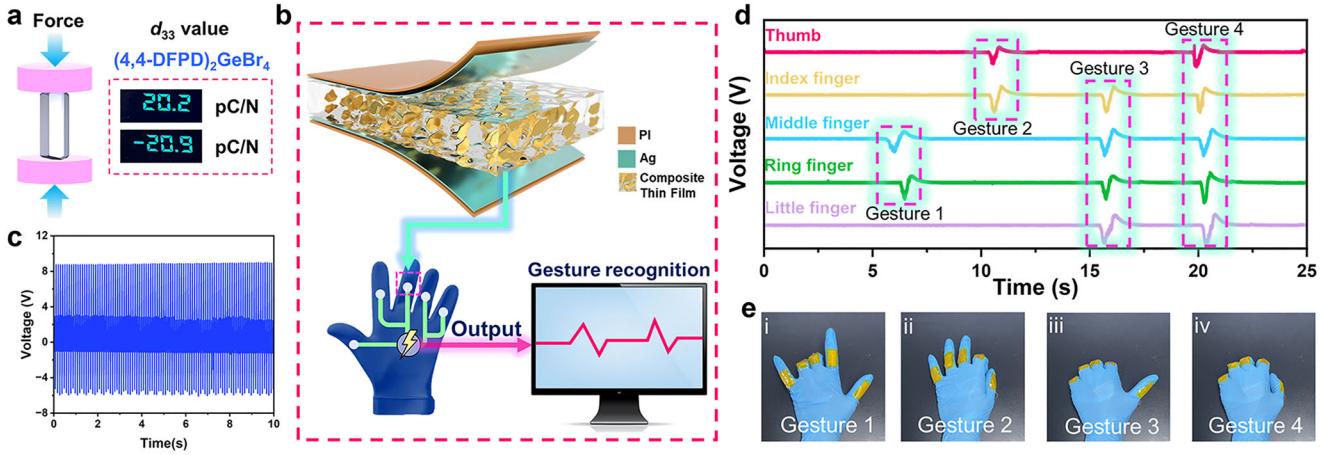

Fig. 6 | Piezoelectric response and sensing output. a The piezoelectric coefficient d_{33} testing through quasi-static method. **b** The diagram of sandwich (4,4-DFPD)$_2$GeBr$_4$@TPU composite film and smart glove for gesture recognition. **c** Piezoelectric voltage output of the (4,4-DFPD)$_2$GeBr$_4$@TPU composite film. **d** The sensing signal output of gesture changing on five different fingers. **e** The different gesture changing from 1 to 4.

Discussion

In summary, our study reports a 2D germanium halide perovskite (4,4-DFPD)$_2$GeBr$_4$ with remarkable comprehensive ferroelectric attributes, including high Curie temperature, large saturation polarization and the strong SHG response as well as multiaxial characteristics of eight equivalent polarization orientations. Revealed by crystal structure analysis and the first-principles calculations, its prominent ferroelectricity is attributed to the synergistic effects of the 4s^2 lone pair expression of Ge^{2+} ions and the ordering of fluorinated 4,4-DFPD cations. (4,4-DFPD)$_2$GeBr$_4$ has been designed by a cationic fluorination strategy, which shows two robust roles: inducing structurally polar alignment to generate ferroelectricity and enhancing molecular dipole moments to enlarge spontaneous polarization. Considering the facile solution processing, easy film-forming and multiaxial characteristics, we further prepared a composite (4,4-DFPD)$_2$GeBr$_4$@TPU device to demonstrate its excellent mechanical flexibility and prominent piezoelectric sensing. This successful example provides an exciting pathway to pursue more superior hybrid ferroelectrics towards the aim of practical applications. More novel emerging hybrid germanium halide perovskites are highly expected to promote new structural paradigms, functional optimization and innovative applications in the near future.

Methods

Crystal synthesis and growth

All reagents and solvents used in this work were obtained from commercial suppliers and were not further purified. GeO_2 (MREDA 99%), piperidinium (Shanghai SCR 98%), 4-fluoropiperidine hydrochloride (MERYER 98%), 4,4-difluoropiperidine hydrochloride (MACKLIN 98%), H_3PO_2 (Chengdu Huaxia 50 wt% in H_2O) and HBr (MERYER 40 wt% in H_2O).

(PD)GeBr$_3$ and (4-FPD)GeBr$_3$ were prepared by a 1:1 molar ratio of GeO_2 and corresponding amine. GeO_2 (2 mmol) was dissolved in excess hydrobromic acid solution (8 mL) and hypophosphorous acid (0.5 mL) at 393 K under stirring for 30 min to reduce Ge^{4+}–Ge^{2+}. 2 mmol organic amine was added when the solution was cooled to 373 K. Then, we turn off the stirring program, the prism-like crystals can be obtained when the solution is slowly cooled to room temperature with a set cooling programmer at a rate of 1 K/h. (PD)GeBr$_3$ forms light brown crystals, whereas (4-FPD)GeBr$_3$ is colorless. We used a glass sand core funnel for filtration to separate the mother liquor from the obtained crystals and rinsed with the apolar solvent toluene. After filtration, we carefully clean the crystal samples with filter paper to remove some of the residual solvent from the surface. Then, the samples were placed in a blast drying oven and dried at 50 °C for 1 h. At last, samples were saved in a dryer filled with color-changing silica gel.

The colorless plate-like (4,4-DFPD)$_2$GeBr$_4$ single samples were prepared by a 2:1 molar ratio of GeO_2 and corresponding organic cations (2 mmol GeO_2 and 4 mmol 4,4-difluoropiperidine hydrochloride). Besides, the synthesis and drying process is the same as for (PD)GeBr$_3$ and (4-FPD)GeBr$_3$.

Preparation of polycrystalline thin film

Thin films were prepared via a drop-coating method. 100 mg of (4,4-DFPD)$_2$GeBr$_4$ crystals were dissolved in 1.5 mL Hydrobromic acid (HBr) under continuous stirring. Indium tin oxide-coated glass substrates were ultrasonically cleaned and subjected to UV-ozone treatment prior to deposition. Subsequently, 100 µL of the precursor solution was deposited onto a temperature-controlled stage preheated to 333 K. Polycrystalline thin films were obtained through annealing for 30 min under ambient conditions.

Preparation of composite thin film and piezoelectric sensing device

The composite films were prepared at a 10% mass ratio of (4,4-DFPD)$_2$GeBr$_4$ to TPU in the precursor solution. 1 g TPU (Thermoplastic polyurethane elastomers) was weighted to dissolved in DMF solvent. Then, 0.1 g (4,4-DFPD)$_2$GeBr$_4$ was weighed and added to the TPU solution and stirred for 2 h. And the solution was poured into a glass substrate and heated to dry in an oven at 333 K for 6 h to prepare a composite film of 10 wt% (4,4-DFPD)$_2$GeBr$_4$@TPU. Silver gel was coated on the top and bottom surfaces of the (4,4-DFPD)$_2$GeBr$_4$@TPU composite as electrodes to form a sandwich structure. Subsequently, the composites were high-voltage polarized at a field strength of 11.5 kV/mm for 12 h. Then, they were encapsulated with insulating polyimide tape to avoid friction electrical interference. Finally, the piezoelectric devices were fixed to the knuckles of the corresponding five fingers on the nitrile gloves with insulated polyimide tape, using enameled copper wires as leads.

Single crystal X-ray determine

Variable-temperature SC-XRD data were obtained using a Bruker D8 Venture diffractometer. The data collection utilized Mo Kα radiation (λ = 0.71073 Å) with the instrument operating at 50 kV and 1.4 mA across various temperatures. The diffraction data was disposed by the APEX3 software. The single-crystal data were solved and refined using

the SHELXTL and OLEX 1.5 software packages, with all non-hydrogen atoms treated anisotropically. Other relevant crystallographic data are listed in Tables S1, S2 and S6. CCDC 2417385-2417388 and 2450159-2450161 for the resulting crystallographic data have been uploaded to www.ccdc.cam.ac.uk/data_request/cif.

Differential scanning calorimetry and dielectric measurements

Single crystal samples were grinded with an agate mortar to obtain polycrystalline powder samples. 7.3 mg polycrystalline powder of (4,4-DFPD)$_2$GeBr$_4$ were weighed for DSC measurement by using a NETZSCH DSC 214 instrument with a rate parameter of 20 K/min and nitrogen atmosphere. Temperature-dependent dielectric constant ε ($\varepsilon = \varepsilon' - i\varepsilon''$, where ε' is the real part of the complex constant and ε'' is the imaginary part) testing on single crystal of (4,4-DFPD)$_2$GeBr$_4$ were carried out on the Tonghui TH2828A over the frequency of 500 Hz to 1 MHz. Both the ends of single crystal were pasted with silver conducting glue.

Ferroelectric (*P-E*) hysteresis loop and PFM characterizations

The measured sample was prepared by coating with conductive silver glue on each side. *P-E* hysteresis loops were measured on the Radiant Precision Premier II with a typical Sawyer-Tower circuit. PFM is based on the atomic force microscopy (AFM), with an alternating current (AC) drive voltage applied to the conductive tip. PFM is a technique derived from AFM that uses an AC drive voltage applied to a conductive tip. Ferroelectric polarization imaging and local switching experiments were conducted by using a resonant-enhanced PFM system (MFP-3D, Asylum Research) equipped with conductive Pt/Ir-coated silicon probes (EFM, Nanoworld).

Second harmonic generation measurements

Single crystals were ground into polycrystalline powders with a mortar for SHG testing. The testing was performed by a pulsed Nd:YAG laser operating at a wavelength of 1064 nm. Polycrystalline powders with particle sizes ranging from 62 to 350 μm were obtained through sieving with varying mesh sizes for SHG phase matching measurement. Crystal samples of (4,4-DFPD)$_2$GeBr$_4$ were used for laser damage threshold testing. A 1064 nm picosecond laser with pump power from 10 to 90 mW was used. We selected a 50X objective lens (N.A = 0.6, Nikon TU Plan ELWD) to focus the different pump power laser onto the sample and collect the SHG signal.

Computational calculations

We extract the organic cations from the measured single crystal structure to construct a molecular conformation. And the dipole moment was calculated at the b3lyp/6-31G level with Gaussian 09W software. For the ferroelectric polarization calculation, more details can be found in Supplementary Note 1.

Calculations of Δd and σ^2_{oct}

The octahedral elongation (Δd) and the octahedral angle variance (σ^2_{oct}) can be evaluated through the following equation: $\Delta d = \frac{1}{6}\sum_{i=1}^{6}\left(\frac{d_n - d}{d}\right)^2$, in which d_n refers to the six individual Ge−Br bond lengths, while d represents represents the average bond length of Ge−Br. $\sigma^2_{oct} = \frac{1}{11}\sum_{i=1}^{12}(\alpha_i - 90)^2$, where α_i is the angle of Br-Ge-Br in the octahedron.

Powder X-ray diffraction

PXRD measurements were carried out on a Bruker D8 Advance instrument under ambient atmosphere. Diffraction patterns were collected in the 2θ range of 5–45° with a step size of 0.02°.

Thermogravimetric testing

Thermogravimetric analysis was performed on the NETZSCH STA449 F5 instrument. The crystal samples of (PD)GeBr$_3$, (4-DFPD)GeBr$_3$ and (4,4-DFPD)$_2$GeBr$_4$ were used to conduct a measurement. Testing was performed in the temperature range of 300–900 K at a heating rate of 10 K min^{-1} under a nitrogen atmosphere.

UV–Vis-NIR measurements

Ultraviolet-Visible-NearInfrared (UV–Vis-NIR) absorption and reflectance spectroscopy were obtained on a Cary RF 6000 instrument. Polycrystalline powders of (4,4-DFPD)$_2$GeBr$_4$ were used for testing at 200–2000 nm with a step size of 1 nm.

Raman spectroscopy

Raman spectroscopy and imaging were performed using a confocal Raman microscope (Alpha300R, WITec, Germany) with a 532 nm single-frequency laser (40 mW, WITec) and a 100× oil immersion objective (NA 0.9, Carl Zeiss, Germany). The backscattered signal was collected through a 50 μm optical fiber and directed to a UHTS 300 spectrometer (300 g.mm^{-1} grating, WITec), with detection by a CCD camera (Andor DU401 BV, UK). Spectra covering 50–4000 cm^{-1} were acquired at 0.5 μm intervals with a 1 s integration time. Data acquisition and mapping were controlled via Control Five and Project Five software (WITec), respectively. Raman images were reconstructed based on the integrated intensities of bands at 1734 cm^{-1} (ester) and 3400 cm^{-1} (hydroxyl).

Reporting summary

Further information on research design is available in the Nature Portfolio Reporting Summary linked to this article.

Data availability

The crystal structures generated in this study have been deposited in the Cambridge Crystallographic Data Centre with reference number of CCDC 2417385-2417388, 2450160-2450161 and 2463567 [www.ccdc.cam.ac.uk/data_request/cif]. Source data are provided with this paper.

References

1. Jena, A. K., Kulkarni, A. & Miyasaka, T. Halide perovskite photovoltaics: background, status, and future prospects. *Chem. Rev.* **119**, 3036–3103 (2019).
2. Wang, R. et al. Prospects for metal halide perovskite-based tandem solar cells. *Nat. Photon.* **15**, 411–425 (2021).
3. Jiang, Q. et al. Surface reaction for efficient and stable inverted perovskite solar cells. *Nature* **611**, 278–283 (2022).
4. Jia, Y., Kerner, R. A., Grede, A. J., Rand, B. P. & Giebink, N. C. Continuous-wave lasing in an organic–inorganic lead halide perovskite semiconductor. *Nat. Photon.* **11**, 784–788 (2017).
5. Wu, H., Ge, Y., Niu, G. & Tang, J. Metal halide perovskites for X-ray detection and imaging. *Matter* **4**, 144–163 (2021).
6. Zheng, W. et al. Emerging halide perovskite ferroelectrics. *Adv. Mater.* **35**, 2205410 (2023).
7. Xu, J. et al. Halide perovskites for nonlinear optics. *Adv. Mater.* **32**, 1806736 (2020).
8. Chouhan, L., Ghimire, S., Subrahmanyam, C., Miyasaka, T. & Biju, V. Synthesis, optoelectronic properties and applications of halide perovskites. *Chem. Soc. Rev.* **49**, 2869–2885 (2020).
9. Luo, M., Tarasov, A., Zhang, H. & Chu, J. Hybrid perovskites unlocking the development of light-emitting solar cells. *Nat. Rev. Mater.* **9**, 295–297 (2024).
10. Lines, M. E. & Glass, A. M. *Principles and Applications of Ferroelectrics and Related Materials* (Oxford University Press, 2001).
11. Scott, J. F. Applications of modern ferroelectrics. *Science* **315**, 954–959 (2007).

12. Dmitriev, V. G., Gurzadyan, G. G. & Nikogosyan, D. N. *Handbook of nonlinear optical crystals* (Springer, 2013).
13. Xue, H. et al. A wearable pyroelectric nanogenerator and self-powered breathing sensor. *Nano Energy* **38**, 147–154 (2017).
14. Yuan, X. et al. Piezoelectricity, pyroelectricity, and ferroelectricity in biomaterials and biomedical applications. *Adv. Mater.* **36**, 2308726 (2024).
15. Ghimire, S. & Klinke, C. Two-dimensional halide perovskites: synthesis, optoelectronic properties, stability, and applications. *Nanoscale* **13**, 12394–12422 (2021).
16. Ji, L.-J., Sun, S.-J., Qin, Y., Li, K. & Li, W. Mechanical properties of hybrid organic-inorganic perovskites. *Coord. Chem. Rev.* **391**, 15–29 (2019).
17. Mao, L., Stoumpos, C. C. & Kanatzidis, M. G. Two-dimensional hybrid halide perovskites: principles and promises. *J. Am. Chem. Soc.* **141**, 1171–1190 (2019).
18. Saparov, B. & Mitzi, D. B. Organic–inorganic perovskites: structural versatility for functional materials design. *Chem. Rev.* **116**, 4558–4596 (2016).
19. He, W. et al. Dion–Jacobson perovskites with a ferroelectrically switchable chiral nonlinear optical response. *J. Am. Chem. Soc.* **147**, 811–820 (2024).
20. Mączka, M. et al. [Methylhydrazinium]$_2$PbBr$_4$, a ferroelectric hybrid organic–inorganic perovskite with multiple nonlinear optical outputs. *Chem. Mater.* **33**, 2331–2342 (2021).
21. Park, I.-H. et al. Ferroelectricity and Rashba effect in a two-dimensional Dion-Jacobson hybrid organic–inorganic perovskite. *J. Am. Chem. Soc.* **141**, 15972–15976 (2019).
22. Park, J. Y. et al. A lead-free ferroelectric 2D Dion–Jacobson tin iodide perovskite. *Adv. Mater.* **36**, 2314292 (2024).
23. Zhang, H.-Y. et al. Large electrostrictive coefficient in a two-dimensional hybrid perovskite ferroelectric. *J. Am. Chem. Soc.* **143**, 1664–1672 (2021).
24. Liu, X. et al. Giant room temperature electrocaloric effect in a layered hybrid perovskite ferroelectric: [$(CH_3)_2CHCH_2NH_3]_2PbCl_4$. *Nat. Commun.* **12**, 5502 (2021).
25. Ma, Y. et al. Unusual triple-state switching of thermally induced birefringence in a two-dimensional perovskite ferroelectric. *J. Am. Chem. Soc.* **146**, 27287–27292 (2024).
26. Chen, X.-G. et al. Two-dimensional layered perovskite ferroelectric with giant piezoelectric voltage coefficient. *J. Am. Chem. Soc.* **142**, 1077–1082 (2020).
27. Shi, P.-P. et al. Symmetry breaking in molecular ferroelectrics. *Chem. Soc. Rev.* **45**, 3811–3827 (2016).
28. Li, W. et al. Chemically diverse and multifunctional hybrid organic–inorganic perovskites. *Nat. Rev. Mater.* **2**, 16099 (2017).
29. Liu, H.-Y., Zhang, H.-Y., Chen, X.-G. & Xiong, R.-G. Molecular design principles for ferroelectrics: ferroelectrochemistry. *J. Am. Chem. Soc.* **142**, 15205–15218 (2020).
30. Zhang, H.-Y., Tang, Y.-Y., Shi, P.-P. & Xiong, R.-G. Toward the targeted design of molecular ferroelectrics: modifying molecular symmetries and homochirality. *Acc. Chem. Res.* **52**, 1928–1938 (2019).
31. Siwach, P., Sikarwar, P., Halpati, J. S. & Chandiran, A. K. Design of above-room-temperature ferroelectric two-dimensional layered halide perovskites. *J. Mater. Chem. A* **10**, 8719–8738 (2022).
32. Ai, Y., Lv, H.-P., Wang, Z.-X., Liao, W.-Q. & Xiong, R.-G. H/F substitution for advanced molecular ferroelectrics. *Trends Chem.* **3**, 1088–1099 (2021).
33. Tang, Y.-Y. et al. Record enhancement of phase transition temperature realized by H/F substitution. *Adv. Mater.* **32**, 2003530 (2020).
34. Chen, X.-G. et al. Confinement-driven ferroelectricity in a two-dimensional hybrid lead iodide perovskite. *J. Am. Chem. Soc.* **142**, 10212–10218 (2020).
35. Xie, Y. et al. The soft molecular polycrystalline ferroelectric realized by the fluorination effect. *J. Am. Chem. Soc.* **142**, 12486–12492 (2020).
36. Peng, Y. et al. Acquiring high-T_C layered metal halide ferroelectrics via cage-confined ethylamine rotators. *Angew. Chem. Int. Ed.* **60**, 2839–2843 (2021).
37. Xu, H. et al. Building block-inspired hybrid perovskite derivatives for ferroelectric channel layers with gate-tunable memory behavior. *Angew. Chem. Int. Ed.* **62**, e202309416 (2023).
38. Shi, C. et al. Two-dimensional organic–inorganic hybrid rare-earth double perovskite ferroelectrics. *J. Am. Chem. Soc.* **142**, 545–551 (2020).
39. Sun, B. et al. Reversible thermochromism and strong ferromagnetism in two-dimensional hybrid perovskites. *Angew. Chem. Int. Ed.* **59**, 203–208 (2020).
40. Zheng, H. et al. Chiral multiferroicity in two-dimensional hybrid organic-inorganic perovskites. *Nat. Commun.* **15**, 5556 (2024).
41. Fu, Y., Jin, S. & Zhu, X. Y. Stereochemical expression of ns2 electron pairs in metal halide perovskites. *Nat. Rev. Chem.* **5**, 838–852 (2021).
42. Morteza Najarian, A. et al. Homomeric chains of intermolecular bonds scaffold octahedral germanium perovskites. *Nature* **620**, 328–335 (2023).
43. Stoumpos, C. C. et al. Hybrid germanium iodide perovskite semiconductors: active lone pairs, structural distortions, direct and indirect energy gaps, and strong nonlinear optical properties. *J. Am. Chem. Soc.* **137**, 6804–6819 (2015).
44. Zhang, Y. et al. Ferroelectricity in a semiconducting all-inorganic halide perovskite. *Sci. Adv.* **8**, eabj5881 (2022).
45. Ding, K. et al. Superior ferroelectricity and nonlinear optical response in a hybrid germanium iodide hexagonal perovskite. *Nat. Commun.* **14**, 2863 (2023).
46. Li, X. et al. Stereo-active lone pairs induced giant polarization in a 2D Ge-based halide perovskite antiferroelectric. *Adv. Funct. Mater.* **34**, 2311944 (2024).
47. Li, X. et al. Two-dimensional layered germanium iodide perovskite ferroelectric semiconductors. *Angew. Chem. Int. Ed.* **64**, e202424058 (2025).
48. Li, X., Guan, Y., Li, X. & Fu, Y. Stereochemically active lone pairs and nonlinear optical properties of two-dimensional multilayered tin and germanium iodide perovskites. *J. Am. Chem. Soc.* **144**, 18030–18042 (2022).
49. Liu, Y. et al. Hybrid germanium bromide perovskites with tunable second harmonic generation. *Angew. Chem. Int. Ed.* **61**, e202208875 (2022).
50. Wang, H. et al. Chiral hybrid germanium(ii) halide with strong nonlinear chiroptical properties. *Angew. Chem. Int. Ed.* **62**, e202309600 (2023).
51. Zhang, H.-Y. et al. Observation of vortex domains in a two-dimensional lead iodide perovskite ferroelectric. *J. Am. Chem. Soc.* **142**, 4925–4931 (2020).
52. Harada, J. et al. Directionally tunable and mechanically deformable ferroelectric crystals from rotating polar globular ionic molecules. *Nat. Chem.* **8**, 946–952 (2016).
53. Ye, H.-Y. et al. Metal-free three-dimensional perovskite ferroelectrics. *Science* **361**, 151–155 (2018).
54. Ai, Y. et al. Unprecedented ferroelectricity and ferromagnetism in a Cr2+-based two-dimensional hybrid perovskite. *Angew. Chem. Int. Ed.* **61**, e202206034 (2022).
55. Wu, Z. et al. Discovery of an above-room-temperature antiferroelectric in two-dimensional hybrid perovskite. *J. Am. Chem. Soc.* **141**, 3812–3816 (2019).
56. Liao, W.-Q. et al. A lead-halide perovskite molecular ferroelectric semiconductor. *Nat. Commun.* **6**, 7338 (2015).

57. Srivastava, P., Maity, S. & Srinivasan, V. Unveiling the role reversal of guest and host in overtolerant hybrid perovskites. *Small* **21**, 2404493 (2025).

Acknowledgements

This work was financially supported by the National Natural Science Foundation of China (22405243 (Z.-X.Z.), 22371258 (D.-W.F.) and 22375182 (Y.Z.)), the Natural Science Foundation of Zhejiang Province (LZ24B010001 (Y.Z.), LQN25B010003 (Z.-X.Z.) and LQN25B010004 (C.-F.W.)) and the Science and Technology Plan Project of Jinhua (2024-1-060) (Z.-X.Z.).

Author contributions

Z.-X.Z., Y.Z. and D.-W.F. conceived the project. H.-F.N. and Y.Z. designed the experiments. P.-Z.H., P.-G.L. and L.P. performed the dielectric and DSC testing. Q.-Q.J. and L.-K.Y. performed *P-E* loops measurements and analysis. H.-F.N. performed the single crystal structure measurements and DFT calculations. Z.-X.Z. and C.-F.W. performed PFM measurements and data analysis. G. T. and Q.-F.Z. performed SHG measurements. Q.-F.Z. performed TG, UV-VIS-NIR spectroscopy and PXRD measurements. H.-F.N., G. T., Q.-F.Z. and J.-Q.L. contributed to data analysis and illustrations. J.-Q.L. prepared the composite thin film and piezoelectric sensing device. Z.-X.Z. and H.-F.N. wrote the manuscript, with inputs from all other authors.

Competing interests

The authors declare no competing interests.

Additional information

Supplementary information The online version contains supplementary material available at https://doi.org/10.1038/s41467-025-63134-6.

Correspondence and requests for materials should be addressed to Zhi-Xu Zhang, Da-Wei Fu or Yi Zhang.

Peer review information *Nature Communications* thanks the anonymous reviewer(s) for their contribution to the peer review of this work. A peer review file is available.